Supplementary Material for "Mesoscopic Models for Electro-hydrodynamic Interactions of Polyelectrolytes"

Dmitry I. Kopelevich, Shujun He, Ryan J. Montes, and Jason E. Butler

S1 Electrophoretic Mobility

The bead electrophoretic mobility μ_0^E was estimated based on experimental data for electrophoretic velocity v_0^E of λ-DNA in the absence of shear (Montes, 2018). The experiments were performed in a channel of length $L_c = 1.8$ cm and cross-section of 100×100 μm^2. Solutions of DNA were diluted to concentrations between 0.2 pM and 1 pM using 0.25X Tris-EDTA (2.5 mM Tris-HCl, 0.25 mM EDTA) buffer and were labelled with fluorescent YOYO-1 dye at a ratio of one dye molecule to four base pairs. Under these conditions, the Debye length was estimated to be $\lambda_D = 5.8$ nm $= 0.030b$.

Figure S1 shows dependence of the electrophoretic velocity $v_0^E = \mu_0^E E$ of λ-DNA on the electric potential $V = EL_c$ in the absence of shear. Fitting the dependence of the electrophoretic velocity on the electric field to a straight line yields $\mu_0^E = 120.7e/\zeta$, where e is the elementary charge and $\zeta = 6\pi\eta a$ is the friction coefficient of a single bead.

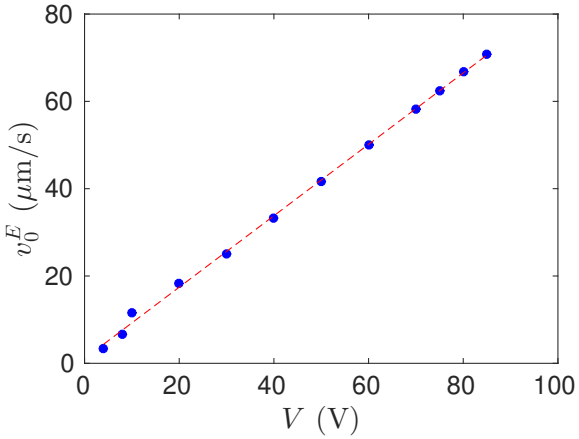

Figure S1: Experimentally determined dependence of the electrophoretic velocity v_0^E of λ-DNA on the electric potential V in the absence of shear, as given by Montes (2018). The dashed line shows results of a least-squares fit of the experimental data to a straight line.

S2 Relaxation Time of the Polymer

There are multiple definitions of the polymer relaxation time τ_r, including the viscous relaxation time and the relaxation times of the end-to-end vector $\boldsymbol{R}(t)$ and distance $R(t)$. Since different definitions yield different values of τ_r (Kekre *et al.*, 2010), it is necessary to choose definition(s) suitable to specific applications. In the current work, the relaxation time τ_r of the polymer is utilized to (i) estimate the time required for the polymer to adjust to a change in the electric field strength and the local shear rate and (ii) compare Weissenberg numbers in our simulations and the experiments of Arca *et al.* (2015).

The first of these applications requires us to choose the definition that corresponds to the largest value of τ_r. As shown by Kekre *et al.* (2010), this is the relaxation time of the end-to-end vector $\boldsymbol{R}(t)$ (in what follows, this relaxation time is denoted as $\tau_r^{(\mathrm{v})}$). On the other hand, to compare the experimental Weissenberg number with the simulations, it is necessary to compute the relaxation time using an approach similar to the one used in experiment. Experimentally, the relaxation time was measured from dynamics of the polymer extension (Gerashchenko & Steinberg, 2008). Therefore, the relevant relaxation time to determine the Weissenberg number is the relaxation time of the end-to-end distance $R(t)$ (in what follows, this relaxation time is denoted as $\tau_r^{(\mathrm{d})}$).

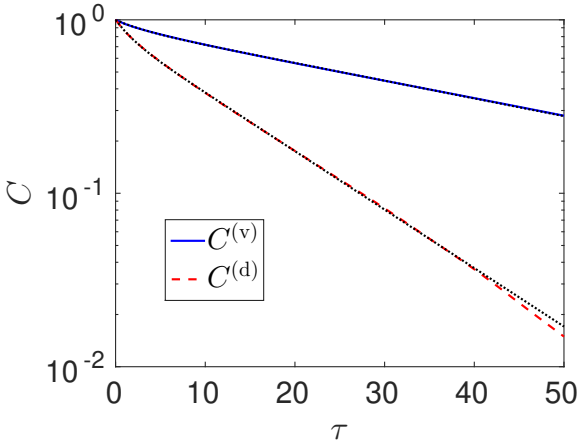

Figure S2: Normalized autocorrelation functions of the polymer at equilibrium. The functions $C^{(\mathrm{v})}$ and $C^{(\mathrm{d})}$ correspond to the end-to-end vector and the end-to-end distance, respectively. The dotted black lines show results of least-squares fits of the autocorrelation functions to the exponential decay law.

The correlations times $\tau_r^{(\mathrm{v})}$ and $\tau_r^{(\mathrm{d})}$ were obtained from the normalized autocorrelation functions of the end-to-end vector $\boldsymbol{R}(t)$,

$$C^{(\mathrm{v})}(\tau) = \frac{\langle \boldsymbol{R}(t) \cdot \boldsymbol{R}(t+\tau) \rangle}{\langle R^2 \rangle}, \tag{S1}$$

and the end-to-end distance $R(t)$,

$$C^{(\mathrm{d})}(\tau) = \frac{\langle R(t) R(t+\tau) \rangle - \langle R \rangle^2}{\langle R^2 \rangle - \langle R \rangle^2}, \tag{S2}$$

of the polymer at equilibrium. These autocorrelation functions are shown in figure S2. It is evident that both of these functions follow the exponential decay law, $\propto \exp(-t/\tau_r)$, and that there is a substantial difference in the decay rate of these functions. Fitting the autocorrelation function $C^{(\mathrm{v})}$ to the exponential decay law, we obtain $\tau_r^{(\mathrm{v})} = 42$. Similarly, fitting the autocorrelation function $C^{(\mathrm{d})}$, we obtain $\tau_r^{(\mathrm{d})} = 12$. Therefore, the Weissenberg number is $\mathrm{Wi} = \gamma\tau_r^{(\mathrm{d})} = 12\gamma$.

In conclusion of this section, we note that the dimensional value of the relaxation time $\tau_r^{(\mathrm{d})}$ is 0.15 s, which differs from the value of 0.1 s used by Arca *et al.* (2015) to compute the Weissenberg number for the experimental system (the latter relaxation time was taken from the experimental work of Gerashchenko & Steinberg (2008)). Therefore, to avoid ambiguity, in comparing the simulations results with the experiments, we matched the shear rates rather than the Weissenberg numbers.

S3 Supplementary Material for Analysis of the Simple Shear Flow

S3.1 Validation of Langevin Equation (2.16)

In this section, we demonstrate that results of Brownian dynamics simulations in a simple shear flow are consistent with the Langevin equation (2.16) for the centre of mass of the polymer. Figure S3 shows a typical example of time-dependence of the mean position $\langle \boldsymbol{R}_c \rangle$ and the mean-squared displacement $\langle \boldsymbol{\xi}_c \boldsymbol{\xi}_c \rangle$ of the polymer centre of mass obtained by Brownian dynamics simulations in a simple shear flow. Here, $\boldsymbol{\xi}_c(t) = \boldsymbol{R}_c(t) - \langle \boldsymbol{R}_c(t) \rangle$. The contribution of the electrophoretic velocity $\mu_0^E E$ is subtracted from the x-component of $\langle \boldsymbol{R}_c(t) \rangle$ in figure S3a to facilitate comparison between electro-hydrodynamic velocities in different directions.

Figure S3a demonstrates that the x- and y-components of the mean polymer position $\langle \boldsymbol{R}_c \rangle$ depend linearly on time (the z-component of $\langle \boldsymbol{R}_c \rangle$ is negligible). This confirms that the mean polymer velocity in a simple shear flow is constant. The xz- and yz-components of the mean-squared-displacement tensor $\langle \boldsymbol{\xi}_c(t) \boldsymbol{\xi}_c(t) \rangle$ (shown in figure S3c) are negligible in comparison with all other components of this tensor. The diagonal components and the xy-component of the tensor $\langle \boldsymbol{\xi}_c(t) \boldsymbol{\xi}_c(t) \rangle$ exhibit a linear dependence on time after some initial transient time t_{tr}. Therefore, for sufficiently large time, the motion of the polymer centre of mass can be described by the Langevin equation (2.16) with constant drift velocity $\boldsymbol{V}_c$ and diffusivity $\boldsymbol{D}$. For the range of parameters considered in the current work, the transient time of the tensor $\langle \boldsymbol{\xi}_c(t) \boldsymbol{\xi}_c(t) \rangle$ is of the same order of magnitude as the relaxation time of the end-to-end vector ($\tau_r^{(\mathrm{v})} \approx 42$, see section S2). As shown in section S4.3.1, this time is sufficiently small to ensure validity of the mean-field model.

It is observed that the off-diagonal xy-component of the tensor $\langle \boldsymbol{\xi}_c(t) \boldsymbol{\xi}_c(t) \rangle$ tends to have a somewhat larger transition time than the diagonal components of this tensor. For the example shown in figure S3, $t_{tr} \approx 20$ for the diagonal tensor components and $t_{tr} \approx 100$ for the xy-component. However, this does not affect validity of the mean-field model. This is because the polymer motion in the x-direction is dominated by the electrophoretic velocity

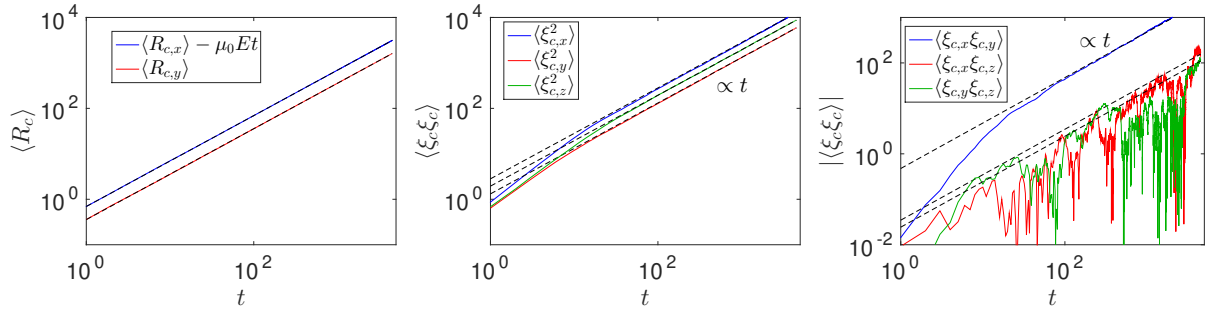

Figure S3: Ensemble averages of the mean position and the mean-squared displacement of the polymer centre of mass obtained by Brownian dynamics simulations of a simple shear flow with the shear rate $\gamma = 0.3$, the electro-hydrodynamic interactions modelled by the long-range model, and the electric field strength $\mathcal{E}_L = 9.41$: (a) mean position $\langle \boldsymbol{R}_c(t) \rangle$ (the z-component of $\langle \boldsymbol{R}_c(t) \rangle$ is negligible and is therefore not shown), (b) diagonal and (c) off-diagonal components of the mean-squared displacement tensor $\langle \boldsymbol{\xi}_c(t) \boldsymbol{\xi}_c(t) \rangle$. The black dashed lines show results of a least-squares fit of individual components of $\langle \boldsymbol{R}_c(t) \rangle$ and $\langle \boldsymbol{\xi}_c(t) \boldsymbol{\xi}_c(t) \rangle$ to linear functions of time. Plot (c) shows the absolute values of $\langle \boldsymbol{\xi}_c(t) \boldsymbol{\xi}_c(t) \rangle$ because the yz- and xz-components of this tensor are negative at some values of t.

$\mu_0^E E$. Hence, the diffusive terms in the x-direction (D_{xx}, D_{xy}, D_{xz}) are neglected in the mean-field model, see Eq. (2.19) and section S4.3.2.

S3.2 Validation of Power-Law Relationships for $V_{c,y}$ and D_{zz}

Power-law relationships between the magnitude of the electric field $\mathcal{E}_m$ and the electro-hydrodynamic drift velocity $V_{c,y}$ in the y-direction and the electro-hydrodynamic dispersion D_{zz} in the z-direction are confirmed in figures S4 and S5, respectively.

S3.3 Molecular Mechanism of Electro-Hydrodynamic Dispersion

Electro-hydrodynamic dispersion arises due to fluctuations of the electro-hydrodynamic velocity, which in turn are caused by fluctuations of the polymer configuration. The latter consist of fast fluctuations of individual beads and slow fluctuations of the molecule as a whole (e.g., tumbling). Relative importance of these dynamics can be assessed by analysis of time-scales of fluctuations of the instantaneous electro-hydrodynamic velocity $\boldsymbol{v}_c^E(t)$ of the polymer center of mass; $\boldsymbol{v}_c^E(t)$ is obtained by averaging electro-hydrodynamic velocities $\boldsymbol{v}_i^E(t)$ of individual beads (given by Eq. (2.9)) at time t. Typical examples of the autocorrelation function of the transverse electro-hydrodynamic velocity $v_{c,y}^E$ of the centre of mass are shown in figure S6. For the long-range model, the autocorrelation function decreases by an order of magnitude within 1 time unit (see figure S6a), which indicates that the dispersion predicted by this model is dominated by fast bead dynamics.

For the short-range model, the relative contribution of the slow polymer dynamics is more significant, especially for weak fields (see figure S6b). Nevertheless, even in this case the

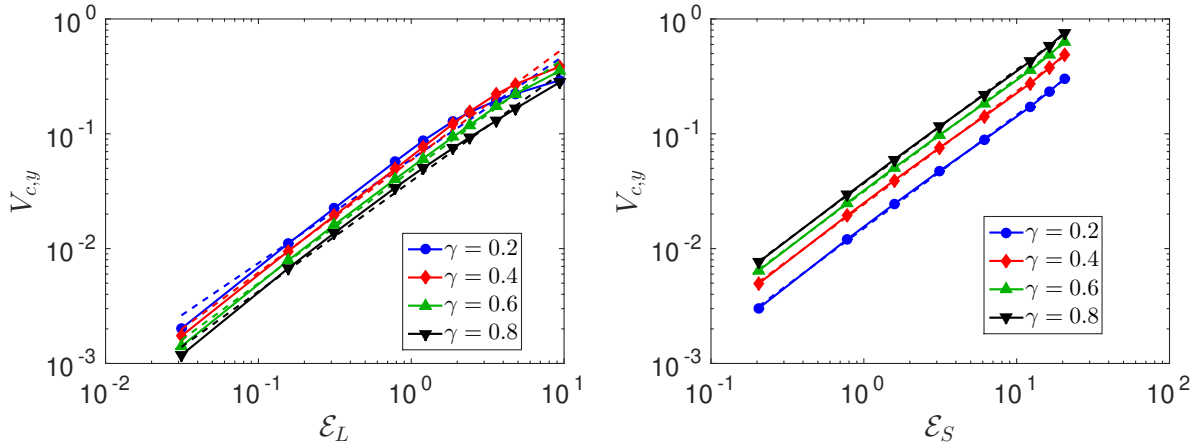

(a) Long-range model (b) Short-range model

Figure S4: Mean polymer velocity $V_{c,y}$ in the y-direction in the simple shear flow obtained by the Brownian dynamics simulations using (a) long-range and (b) short-range models. The dashed lines show results of the fit to the power law $V_{c,y} \propto \mathcal{E}_m^p$.

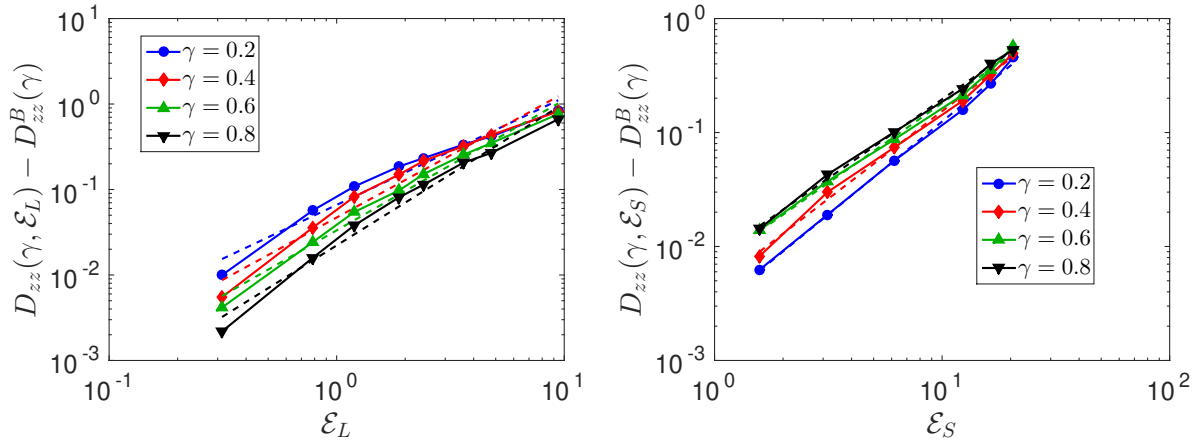

(a) Long-range model (b) Short-range model

Figure S5: Contribution of the electro-hydrodynamic dispersion to the polymer diffusivity in the z-direction obtained by the Brownian dynamics simulations in the simple-shear flow. The dashed lines show results of the fit of the data to the empirical relationship $D_{zz}(\gamma, \mathcal{E}_m) = D_{zz}^B(\gamma) + D_{zz}^E(\gamma)\mathcal{E}_m^{q(\gamma)}$.

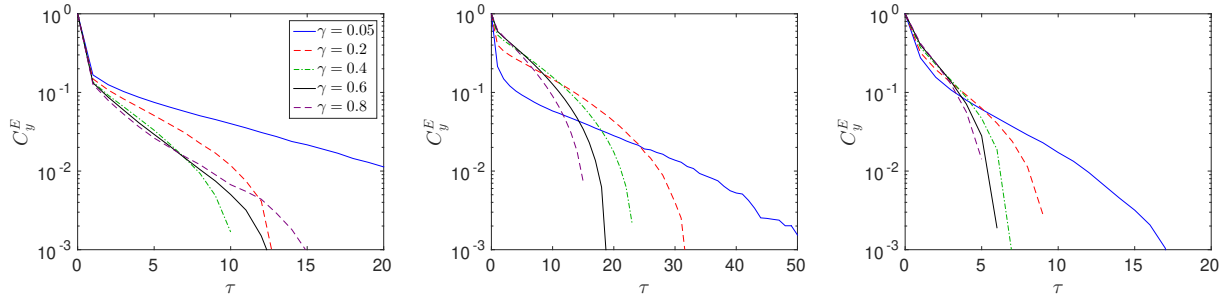

(a) (b) (c)

Figure S6: Autocorrelation functions $C_y^E(\tau)$ of the transverse electro-hydrodynamic velocity $v_{c,y}^E$ obtained from the Brownian dynamics simulations in a simple shear flow: (a) long-range model, $\mathcal{E}_L = 1.19$, (b) short-range model, $\mathcal{E}_S = 1.58$, and (c) short-range model, $\mathcal{E}_S = 16.40$. All autocorrelation functions are normalized so that $C_y^E(0) = 1$.

electro-hydrodynamic fluctuations are dominated by fast fluctuations. This is also evident from plots of the instantaneous transverse velocities $v_{c,y}^E$ shown in figure S7a and b. To further demonstrate that the slow dynamics of polymer configuration as a whole plays a relatively small role in dispersion, we explore effects of polymer tumbling on fluctuations of $v_{c,y}^E$. To this end, we consider dynamics of the orientation $\cos\theta$ of the end-to-end vector $\boldsymbol{R}$ with respect to the flow direction. The sign of the orientation indicates which of the beads (the first or the last one) leads the flow. Of course, the designation of the first and the last beads is arbitrary, but the same designation is kept throughout each simulation, so that the change in sign of the orientation reflects a swap in the beads leading the flow.

Typical tumbling dynamics are shown in figure S7c and d. At high shear rate, the polymer is nearly aligned with the flow (i.e., its orientation is close to +1 or -1) most of the time and once in a while the orientation flips quickly between these two values, see figure S7d. The timescale of this tumbling dynamics is comparable with the relaxation timescale of the end-to-end vector and is much slower than the timescale of the fluctuations of the electro-hydrodynamic velocity $v_{c,y}^E$. The magnitude of the correlation coefficient between the polymer orientation and $v_{c,y}^E$ is less than 0.1, which further confirms that the tumbling dynamics plays a relatively small role in electro-hydrodynamic dispersion.

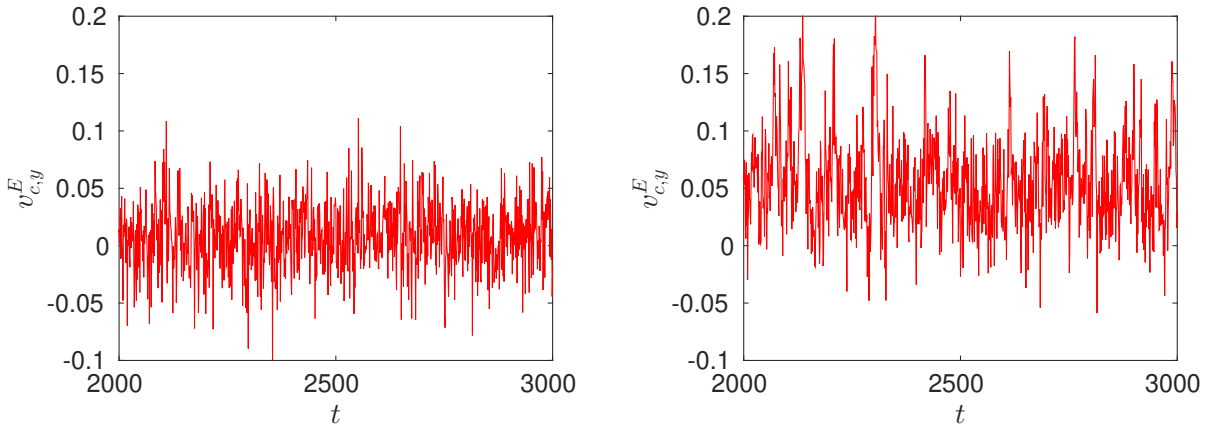

(a) $\gamma = 0.05$

(b) $\gamma = 0.8$

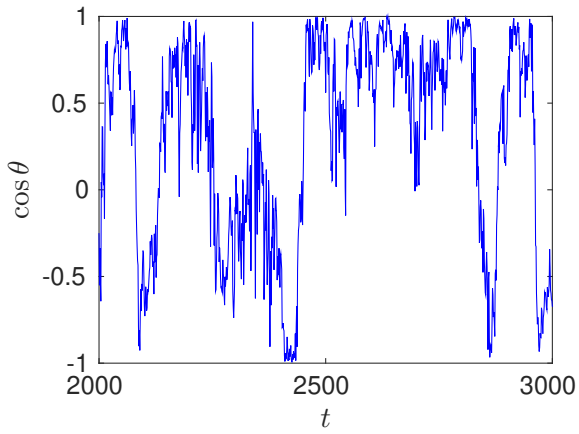

(c) $\gamma = 0.05$

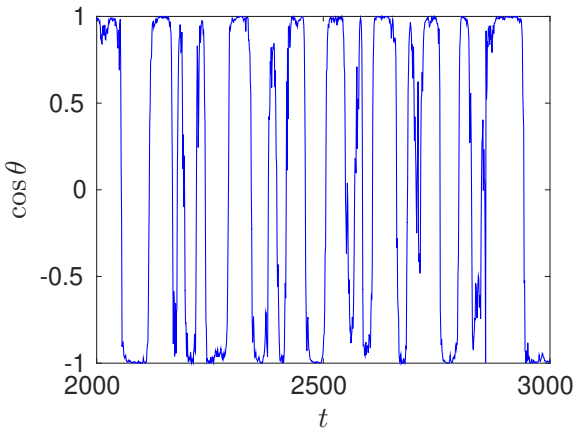

(d) $\gamma = 0.8$

Figure S7: Examples of dynamics of (a), (b) instantaneous electro-hydrodynamic velocity $v^E_{c,y}$ and (c), (d) instantaneous orientation $\cos\theta$ of the end-to-end vector. These trajectories were obtained with the short-range model, a relatively weak electric field ($\mathcal{E}_S = 1.58$), and simple shear flows with the shear rates of (a),(c) $\gamma = 0.05$ and (b),(d) $\gamma = 0.8$. The plots of $v^E_{c,y}$ and $\cos\theta$ at the same shear rate γ are taken from the same segment of the same Brownian dynamics simulation.

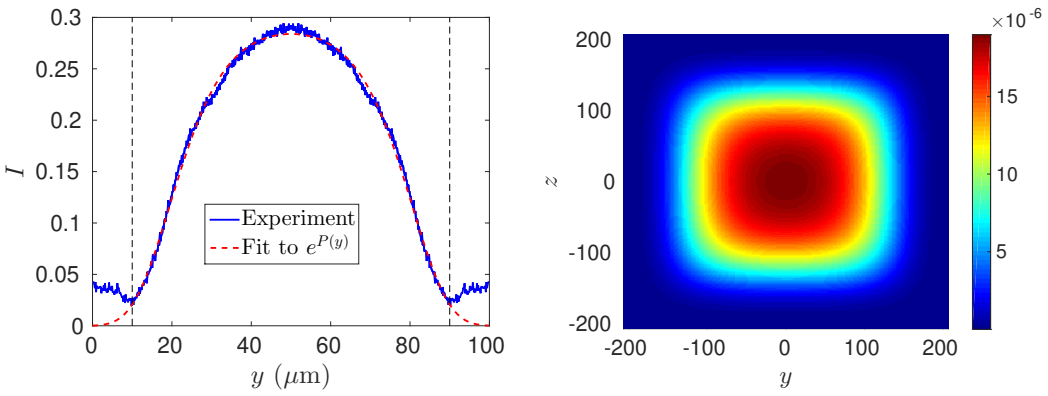

Figure S8: (a) Experimentally measured fluorescence intensity of DNA labelled by dye YOYO-1 near the channel inlet (Montes, 2018). Initial conditions for the simulations were obtained by fitting the experimental data to $e^{P(y)}$ in the interval between the dashed black lines ($P(y)$ is a polynomial of the 6-th degree). (b) Initial conditions for simulations in a channel with a square cross-section.

S4 Supplementary Material for Analysis of the Pressure-Driven Flow

S4.1 Initial Conditions for the Pressure-Driven Flow Obtained from Experimental Data

In addition to the uniform initial conditions, we utilized initial conditions extracted from experimental concentration profiles near the channel inlet (2 mm from the channel entrance). The experiments (Montes, 2018) were performed with fluorescently labelled λ-DNA with the centre-line velocity of 1200 μm/s and the electrophoretic velocity of 200 μm/s in a channel with 100×100 μm^2 cross-section.

The fluorescence intensity profile obtained experimentally was smoothed by fitting it to a function of the form

$$I(y) = Ae^{P(y)}, \tag{S3}$$

where $P(y)$ is a polynomial of the 6-th degree. The image intensity tends to increase near channel walls due to an imaging artifact (Arca *et al.*, 2015). Therefore, only the data away from the walls (10 to 90 μm) were considered in the fit to Eq. (S3). The experimentally measured intensity and results of the fit to Eq. (S3) are shown in figure S8a. Thus obtained concentration profile $C_0(y) \propto e^{P(y)}$ was rescaled to fit the dimensions of the channel considered in the simulations. Initial conditions for 3D simulations in a channel with a square cross-section were computed as $C_{3D}(y, z) = C_0(y)C_0(z)$ and are shown in figure S8b.

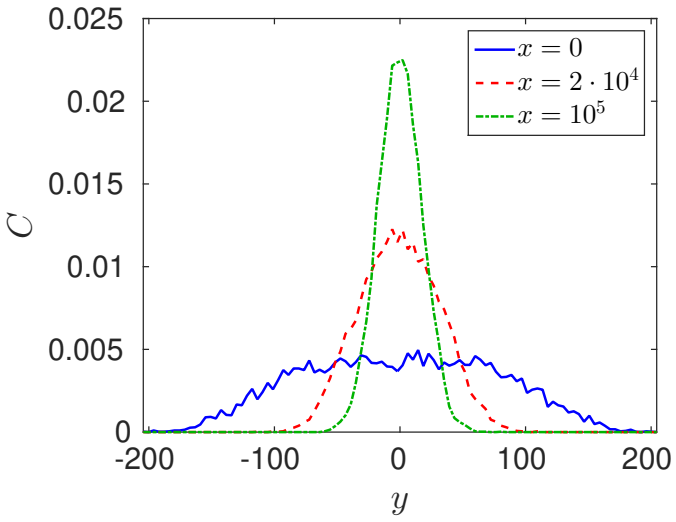

Figure S9: Concentration profiles in a 2D pressure-driven flow at various positions x along the channel obtained by the Brownian dynamics simulations with initial conditions determined from experiment (Montes, 2018). The data shown were obtained using the long-range electrohydrodynamic model at the electric field strength $\mathcal{E}_L = 9.41$ and the mean shear rate $\bar{\gamma} = 0.146$. Positions $x \geq 10^5$ correspond to the developed profile, which is consistent with the developed profile obtained with the uniform initial conditions, see figure 6.

S4.2 Concentration Profiles in Pressure-Driven Flows

Typical snapshots of the concentration profiles obtained from Brownian dynamics simulations of pressure-driven flows in the 2D and 3D channels are shown in Figs. S9 and S10, respectively. It is observed that the developed profiles are independent of the initial conditions. This is further confirmed by figure S11 which shows dependence of the width σ of the concentration profiles on position x along the channel length. Therefore, unless stated otherwise, we focus on results obtained with initial conditions determined from the experimental data.

Two- and three-dimensional flows are compared in figure S12. It is observed that the 2D flows yield slightly narrower profiles. However, overall, the 2D and 3D flows yield very similar results.

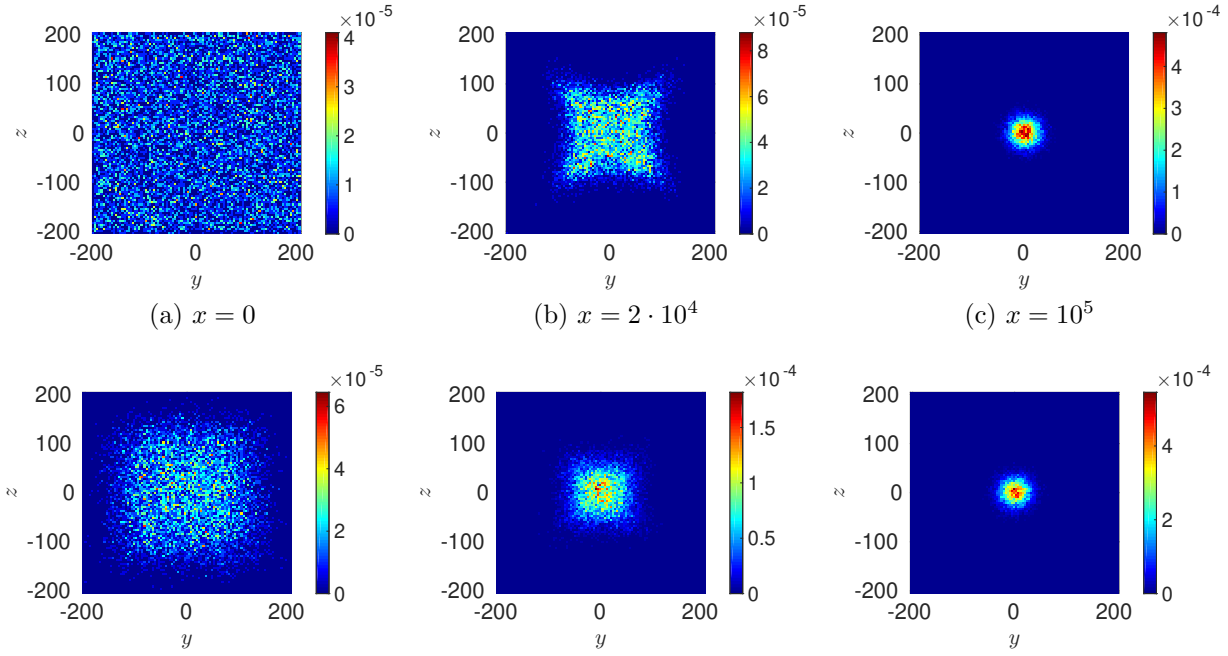

(a) $x = 0$ (b) $x = 2 \cdot 10^4$ (c) $x = 10^5$

(d) $x = 0$ (e) $x = 2 \cdot 10^4$ (f) $x = 10^5$

Figure S10: Concentration profiles in a 3D pressure-driven flow at various positions x along the channel obtained by the Brownian dynamics simulations. The top and bottom rows show, respectively, the results obtained with the uniform initial conditions and the initial conditions determined from experiment (Montes, 2018). The shown data were obtained using the long-range electro-hydrodynamic model at the electric field strength $\mathcal{E}_L = 9.41$ and the mean shear rate $\bar{\gamma} = 0.146$. Positions $x \geq 10^5$ corresponds to the developed profile.

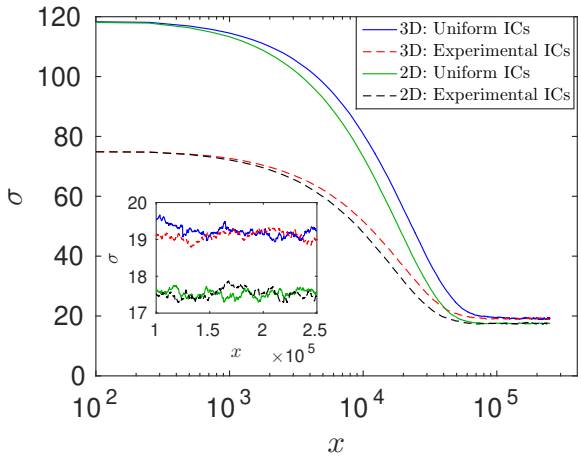

Figure S11: Dependence of widths $\sigma(x)$ of the concentration profiles on position x along the channel in the 2D and 3D pressure-driven flows. The solid and dashed lines show, respectively, the results obtained with the uniform initial conditions (ICs) and the initial conditions determined from experiment (Montes, 2018). The shown data were obtained by the Brownian dynamics simulations using the long-range electro-hydrodynamic model at $\mathcal{E}_L = 9.41$ and $\bar{\gamma} = 0.146$. The inset shows a magnified area corresponding to developed profiles.

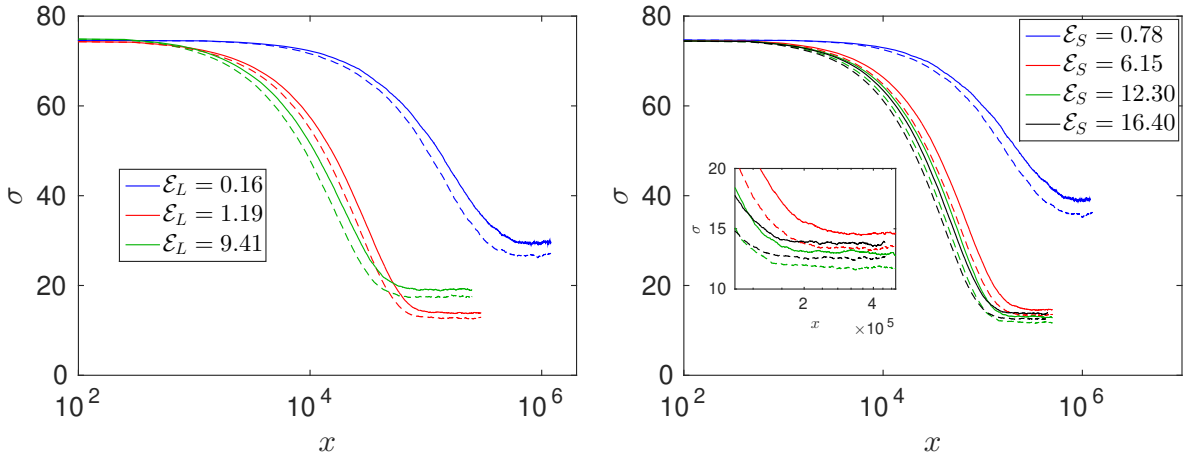

(a) Long-range model

(b) Short-range model

Figure S12: Dependence of widths σ of the concentration profiles on position x along the channel in 3D (solid lines) and 2D (dashed lines) pressure-driven flows. The data were obtained by the Brownian dynamics simulations at $\bar{\gamma} = 0.146$ using (a) long-range and (b) short-range electro-hydrodynamic models. The inset in plot (b) shows a magnified area corresponding to developed profiles for $\mathcal{E}_S = 6.15, 12.30$, and 16.40.

S4.3 Additional Validation of the Mean-Field Model

S4.3.1 Estimation of Time-scales

In this section we demonstrate that in the considered pressure-driven flows the polymer adjusts to its local environment faster than it travels in the transverse direction. The polymer response time τ_r can be estimated as the correlation time $\tau_r^{(\mathrm{v})}$ of the end-to-end vector of a polymer at equilibrium (about 42 for the polymers considered in the current work, see section S2). This timescale is comparable with the timescale of relaxation of fluctuations of the transverse electro-hydrodynamic velocity $v_{c,y}^E$. As shown in figure S6, autocorrelation functions of $v_{c,y}^E$ decay by about 90% within 1 time unit and by more than 99% within $\tau_r = 42$.

The distance travelled in the transverse direction during time τ_r is $V_{c,y}\tau_r$ and the diffusive length-scale is $(D_{yy}\tau_r)^{1/2}$. From the simple shear simulations, we find that, within the range of $\mathcal{E}_L$, $\mathcal{E}_S$, and γ considered in the current work, $V_{c,y} \leq O(1)$ and $D_{yy} = O(1)$. Therefore, both the drift and diffusive length-scales are $O(10)$. The shear rate change corresponding to this distance (assuming a simple parabolic flow) is $\Delta\gamma = 4\bar{\gamma}\Delta y/H$, where $\Delta y = O(10)$ is the distance in the transverse direction travelled by the polymer. Since $H = O(100)$ and $\bar{\gamma} = O(0.1)$, we conclude that $\Delta\gamma = O(10^{-2})$. Therefore, the change in the shear rate corresponding to the distance travelled during the relaxation time of the polymer is relatively small and changes in the polymer environment occur on a slower time-scale than the polymer relaxation time-scale. This justifies the mean-field model assumption.

S4.3.2 Negligible Contribution of Diffusive Transport in x-Direction.

One of the assumptions in the derivation of the mean-field model Eq. (2.19) from Eq. (2.18) is that the terms containing components D_{xx}, D_{xy}, and D_{xz} of the diffusion tensor $\boldsymbol{D}$ are negligible. In this section we verify this assumption.

Components of the diffusive flux $\boldsymbol{j}^D$ are

$$j_x^D = -D_{xx}\frac{\partial C}{\partial x} - D_{xy}\frac{\partial C}{\partial y}, \tag{S4}$$

$$j_y^D = -D_{xy}\frac{\partial C}{\partial x} - D_{yy}\frac{\partial C}{\partial y}, \tag{S5}$$

$$j_z^D = -D_{zz}\frac{\partial C}{\partial z}. \tag{S6}$$

In writing Eqs. (S4) - (S6), we neglected the terms containing D_{xz} and D_{yz}, since those components of the diffusion tensor are negligible in comparison with D_{xx}, D_{xy}, D_{yy}, and D_{zz} (see figure S3). The diagonal components of $\boldsymbol{D}$ have the same order of magnitude. The off-diagonal component D_{xy} is several orders of magnitudes smaller than the diagonal components at low $\mathcal{E}_m$. However, at high $\mathcal{E}_m$ the magnitude of D_{xy} approaches that of the diagonal components, especially in the case of the short-range model (see figure S13 for comparison between D_{xx} and D_{xy}).

Nevertheless, the off-diagonal component makes a negligible contribution to the y-component of the diffusive flux even at high $\mathcal{E}_m$ because gradients of the polymer concentration C in the x- and y-direction differ by two orders of magnitude. The length-scale in the x-direction

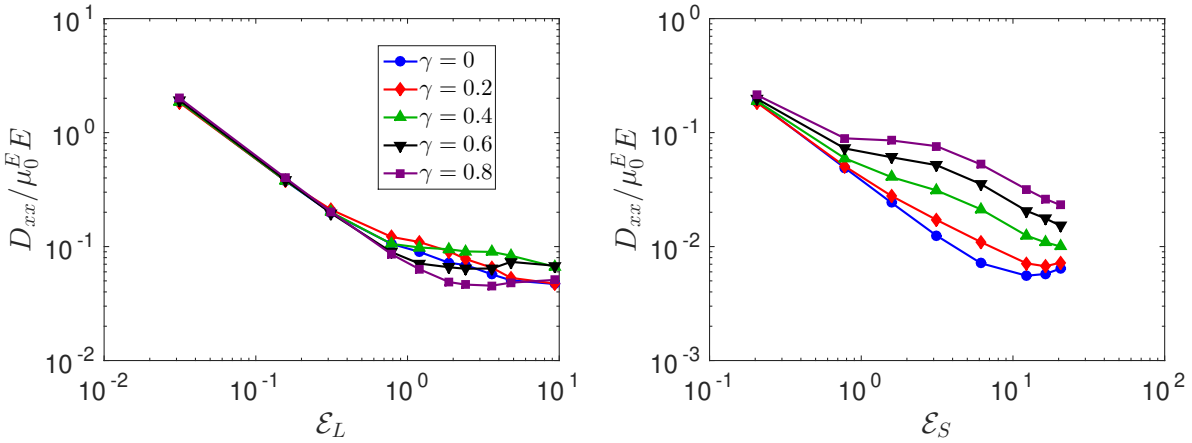

(a) Long-range model

(b) Short-range model

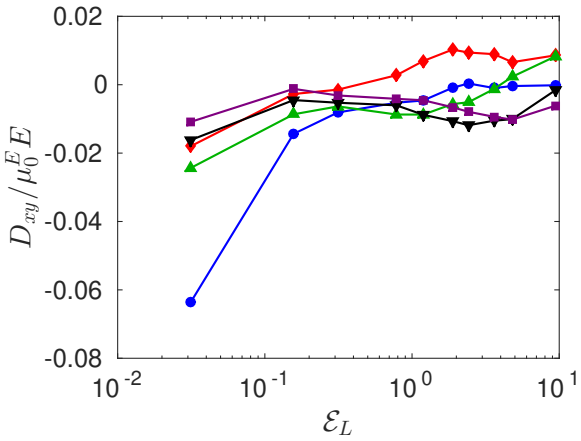

(c) Long-range model

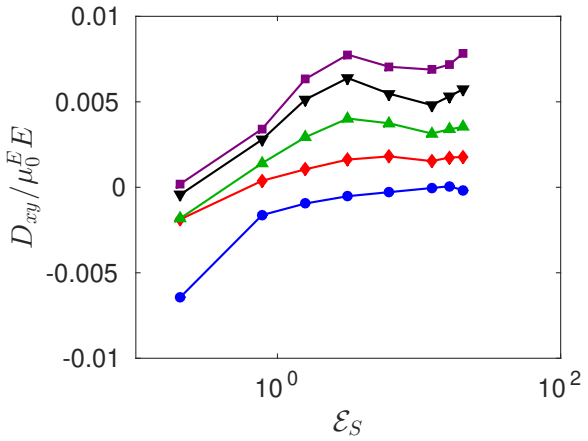

(d) Short-range model

Figure S13: Ratio of components D_{xx} (plots (a), (b)) and D_{xy} (plots (c), (d)) of the diffusivity tensor and the electrophoretic velocity $\mu_0^E E$. The data were obtained by the Brownian dynamics simulations in the simple-shear flow using the long-range model (plots (a),(c)) and the short-range model (plots (b),(d)).

is $O(10^4)$ (see figures 7, S11, and S12), whereas the length-scale in the y-direction is $O(10^2)$ (see figure 6). Therefore,

$$\frac{\partial C}{\partial x} = O(10^{-4})C \quad \text{and} \quad \frac{\partial C}{\partial y} = O(10^{-2})C \tag{S7}$$

and the first term in Eq. (S5) is negligible in comparison with the second term, i.e.

$$j_y^D \approx D_{yy}\frac{\partial C}{\partial y}. \tag{S8}$$

It remains to demonstrate that the diffusive flux in the x-direction is negligible in comparison with the electrophoretic flux

$$j_x^E = \mu_0^E E C. \tag{S9}$$

Using Eq. (S7), the ratio of these fluxes can be estimated as

$$\left|\frac{j_x^D}{j_x^E}\right| = O(10^{-4})\frac{D_{xx}}{\mu_0^E E} + O(10^{-2})\frac{D_{xy}}{\mu_0^E E}, \tag{S10}$$

The ratios $D_{xx}/\mu_0^E E$ and $D_{xy}/\mu_0^E E$ are shown in figure S13. It is evident that $D_{xx}/\mu_0^E \leq O(1)$ and $|D_{xy}|/\mu_0^E \leq O(10^{-2})$. Therefore, $|j_x^D/j_x^E| \leq O(10^{-4})$ and j_x^D can be neglected in the mean-field model.

S4.3.3 Direct Validation for the 3D flow

The mean-field model for the 3D flow is validated by comparison with the Brownian dynamics simulations in figure S14. The mean-field model predictions (dashed lines) are in excellent agreement with the Brownian dynamics results (solid lines).

S4.4 Effect of Electric Field Strength and Mean Shear Rate on the Entrance Length

The entrance length L required to establish a developed profile can be estimated as the ratio of the mean velocities in the longitudinal and transverse directions,

$$L \sim \frac{\bar{u}_x^\infty + \mu_0^E E}{\bar{V}_{c,y}} \tag{S11}$$

Here, u_x^∞ is the ambient flow velocity, $\mu_0^E E$ is the electrophoretic velocity, $V_{c,y}$ is the mean electro-hydrodynamic velocity in the transverse direction, and the bar denotes averaging over the channel cross-section. The electro-hydrodynamic velocity $V_{c,x}$ in the flow direction is neglected in the numerator of Eq. (S11) since $V_{c,x} << \mu_0^E E$. Furthermore, the estimate (S11) neglects variation of the flow and electro-hydrodynamic velocities across the channel, as well as effects of the Brownian diffusion and the electro-hydrodynamic dispersion. Nevertheless, it allows us to qualitatively explain the simulation results discussed below.

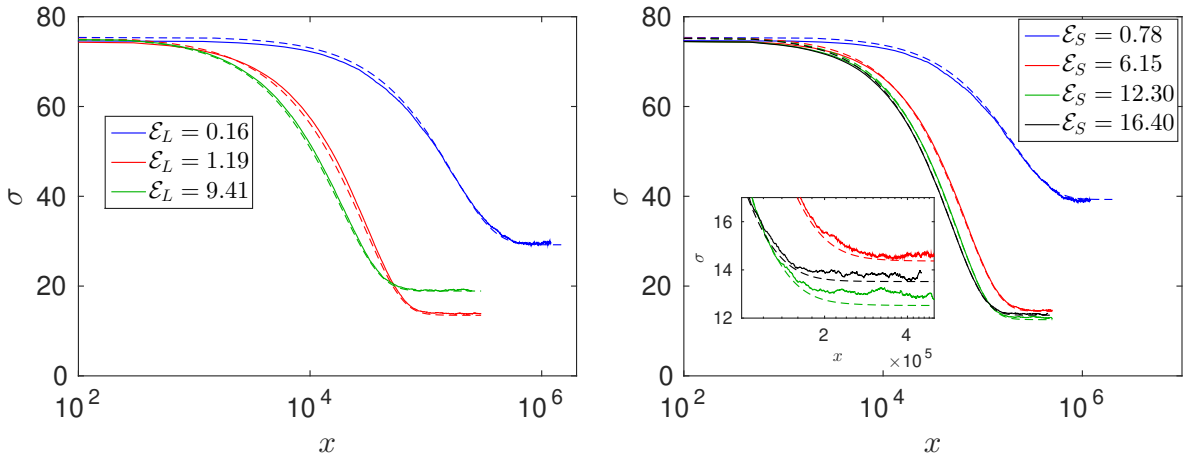

(a) Long-range model

(b) Short-range model

Figure S14: Validation of the mean-field model for the 3D pressure-driven flow. This figure compares $\sigma(x)$ for this flow obtained by the Brownian dynamics simulations (solid lines) and the mean-field model (dashed lines) at $\bar{\gamma} = 0.146$ using (a) long-range and (b) short-range electro-hydrodynamic models. The inset in plot (b) shows a magnified area corresponding to developed profiles for $\mathcal{E}_S = 6.15, 12.30$, and 16.40.

We consider simulations of the mean-field model in the two-dimensional geometry; the initial condition for these simulations is the uniform polymer distribution. The entrance length L computed from these simulations is defined as the distance required to reduce $\Delta\sigma(x)$ by 90%, i.e.

$$\Delta\sigma(L) = 0.1\Delta\sigma(0). \tag{S12}$$

Here, $\Delta\sigma(x) = \sigma(x) - \sigma^\infty$ is the difference between the profile width $\sigma(x)$ at position x and the fully developed profile width σ^∞.

Effects of the electric field strength on the entrance length are shown in figure S15. The long- and short-range electro-hydrodynamic models yield qualitatively similar dependence of L on the electric field strength $\mathcal{E}_m$. This is explained by the estimate (S11): since $\bar{u}_x^\infty$ is independent of $\mathcal{E}_m$ and both considered electro-hydrodynamic models predict that $\bar{V}_{c,y}$ is approximately proportional to $\mathcal{E}_m$ (see figure S4), Eq. (S11) yields

$$L \sim A + \frac{B}{\mathcal{E}_m}, \tag{S13}$$

where A and B are independent of $\mathcal{E}_m$. Results of a least-squares fit of the simulation data to Eq. (S13) are shown by dashed lines in figure S15. It is evident that Eq. (S13) is in good agreement with the entrance length obtained from the simulations.

Effects of the shear rate on the entrance length are shown in figure S16a. Both the long- and short-range models predict that L increases as the mean shear rate $\bar{\gamma}$ increases. This is consistent with the estimate (S11). To verify this, we note that the electrophoretic velocity $\mu_0^E E$ is negligible in comparison with the mean flow velocity $\bar{u}_x^\infty = \bar{\gamma}H/3$ for the systems shown in figure S16: for the considered range of $\bar{\gamma}$, $\bar{u}_x^\infty$ ranges from 14 to 207, whereas

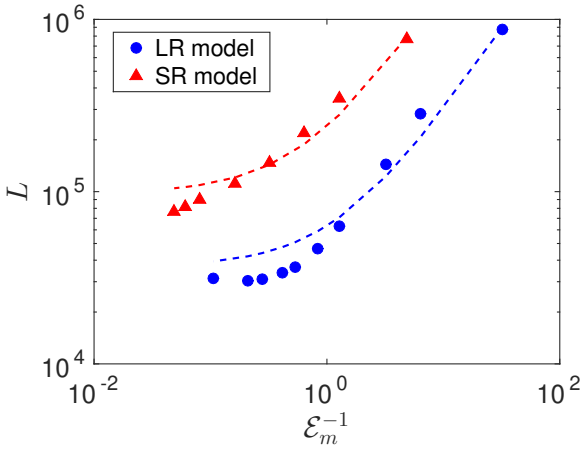

Figure S15: Effect of the strength of the electric field $\mathcal{E}_m$ on the decay length L predicted by the long-range (LR) and the short-range (SR) electro-hydrodynamic models. The shown data are obtained from the mean-field model simulations of a pressure-driven flow in a two-dimensional channel at the mean shear rate of $\bar{\gamma} = 0.146$. The dashed lines show results of a least-squares fit of the simulation data to Eq. (S13).

the largest electrophoretic velocity for the systems considered in figure S16 is $\mu_0^E E = 6$. Therefore, Eq. (S11) can be approximated as

$$L \sim \frac{\bar{u}_x^\infty}{\bar{V}_{c,y}} = \frac{\bar{\gamma} H}{3 \bar{V}_{c,y}} \tag{S14}$$

for sufficiently large $\bar{\gamma}$.

Dependence of the average electro-hydrodynamic velocity $\bar{V}_{c,y}$ on $\bar{\gamma}$ is shown in figure S16b. For the short-range model, $\bar{V}_{c,y} \propto \bar{\gamma}^{0.6}$. Substituting this into Eq. (S14) yields $L \propto \bar{\gamma}^{0.4}$, which is in a reasonable agreement with the simulations results shown in figure S16a ($L \propto \bar{\gamma}^{0.6}$ for $\mathcal{E}_S = 0.21$ and $L \propto \bar{\gamma}^{0.3}$ for $\mathcal{E}_S = 1.58$).

The long-range model exhibits a non-monotonic dependence of the transverse velocity $V_{c,y}(\gamma)$ on the shear rate γ, as discussed in section 3.1 of the paper. Therefore, the transverse velocity $\bar{V}_{c,y}$ averaged over the channel width also exhibits a non-monotonic dependence on the mean shear rate $\bar{\gamma}$, as shown in figure S16b: $\bar{V}_{c,y}(\bar{\gamma})$ approaches a maximum at $\bar{\gamma} \approx 0.25$ and follows the power law $\bar{V}_{c,y} \propto \bar{\gamma}^{-0.3}$ for $\bar{\gamma} \geq 0.25$. Therefore, Eq. (S14) yields $L \propto \bar{\gamma}^{1.3}$ for $\bar{\gamma} \geq 0.25$. This is in good agreement with the mean-field simulations results shown in figure S16a ($L \propto \bar{\gamma}^{1.6}$ for $\mathcal{E}_L = 0.16$ and $L \propto \bar{\gamma}^{1.5}$ for $\mathcal{E}_L = 1.19$).

In summary, dependence of the entrance length L on the mean shear rate $\bar{\gamma}$ can be explained by the simple approximation (S11). The long-range model exhibits a stronger dependence of L on $\bar{\gamma}$ than the short-range model due to the qualitative difference in the effect of the shear rate on the mean transverse velocities predicted by these models (see figure S16b).

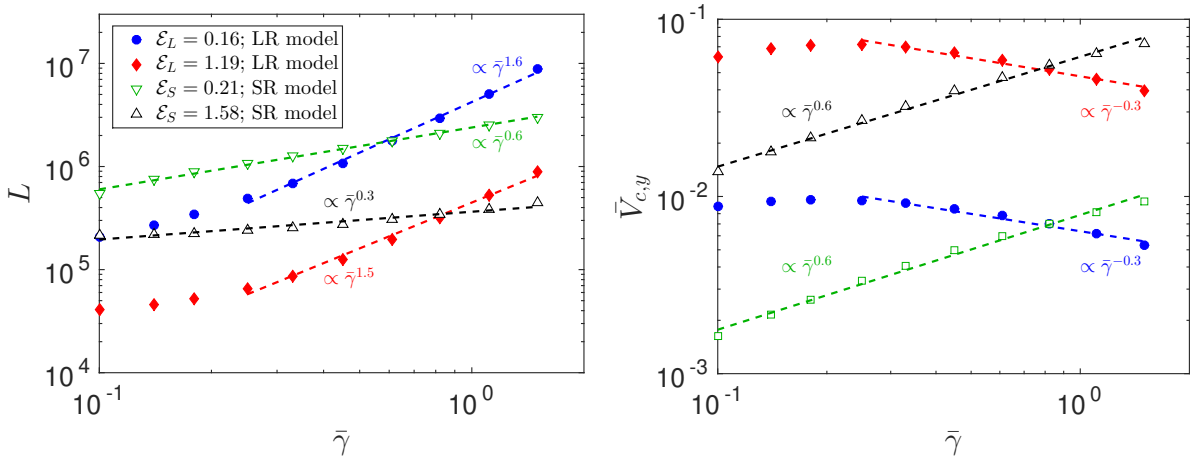

(a) (b)

Figure S16: (a) Effect of the mean shear rate $\bar{\gamma}$ on the decay length L predicted by the long-range (LR) and the short-range (SR) electro-hydrodynamic models. The shown data are obtained from the mean-field model simulations of a pressure-driven flow in a two-dimensional channel. (b) Dependence of the transverse velocity $\bar{V}_{c,y}$ averaged over the channel width on the mean shear rate $\bar{\gamma}$. The dashed lines show results of least-squares fits of the data to the power law. For the long-range model, the fits were performed for $\bar{\gamma} \geq 0.25$.

References

Arca, M., Butler, J. E. & Ladd, A. J. C. 2015 Transverse migration of polyelectrolytes in microfluidic channels induced by combined shear and electric fields. *Soft Matter* **11** (22), 4375–4382.

Gerashchenko, S. & Steinberg, V. 2008 Critical slowing down in polymer dynamics near the coil-stretch transition in elongation flow. *Phys. Rev. E* **78**, 040801(R).

Kekre, R., Butler, J. E. & Ladd, A. J. C. 2010 Comparison of Boltzmann and Brownian Dynamics simulations of polymer migration in confined flows. *Phys. Rev. E* **82**, 011802.

Montes, R. J. 2018 Microfluidic concentration and purification of DNA due to electro-hydrodynamic migration. PhD thesis, University of Florida.